Thermo-Mechanical FEM Study of SMAW Parameter Effects in S355J2+N / ASTM A572 Gr.50 Dissimilar Steel Joints

Estudio termomecánico mediante el método de elementos finitos de los efectos de los parámetros de la soldadura SMAW en uniones de aceros disímiles S355J2+N / ASTM A572 Gr.50.

Estudo termomecânico por elementos finitos dos efeitos dos parâmetros de soldagem SMAW em juntas de aços dissimilares S355J2+N / ASTM A572 Gr.50

Syed Farrukh Haider [1], Shaheryar A. Khan [2] (*), Aqueel Shah [3], Muhammad Nasir Bashir [4], Asif Mansoor [5],
Abbas Hussain [6], M. Mahmood Ali [7], Salman Nisar [8]

Recibido: 09/09/2025 Aceptado: 24/11/2025

Summary. - Shielded Metal Arc Welding (SMAW) is widely employed in structural steel fabrication; however, the thermo-mechanical response of dissimilar structural steel joints remains insufficiently explored through numerical modeling. In this study, a three-dimensional transient thermo-mechanical finite element model is developed to investigate SMAW of dissimilar S355J2+N and ASTM A572 Grade 50 steel plates. Goldak's double-ellipsoidal heat source is implemented to represent arc heat input, and a Box–Behnken design is employed to systematically examine the influence of welding current, voltage, and travel speed. The analysis focuses on peak temperature, out-of-plane distortion, and elastic stress indicators derived from a linear thermo-elastic formulation. The results indicate that welding current predominantly governs peak temperature, while travel speed has the strongest influence on thermal gradients and distortion behavior; voltage exhibits a secondary but non-negligible effect on heat distribution. Simulated thermal and deformation trends are benchmarked against published experimental and numerical studies on comparable structural steels and show consistent qualitative behavior. Owing to the absence of plasticity, temperature-dependent material properties, and direct experimental validation, stress results are interpreted solely as qualitative indicators rather than physically realistic residual stresses. The study provides a structured thermo-elastic FEM and design-of-experiments–based sensitivity framework for a dissimilar structural steel combination not previously reported in SMAW numerical studies, offering practical insight into parameter screening for thermal and distortion control in structural steel fabrication.

(*) Corresponding author.

[1] Postgraduate Student, National University of Sciences and Technology (Pakistan), syedhaider270@yahoo.com,
ORCID iD: https://orcid.org/0009-0007-2560-2664

[2] Associate Professor and Head of the Department of Mechanical Engineering., DHA Suffa University (Pakistan), shaheryar.atta@dsu.edu.pk,
ORCID iD: https://orcid.org/0000-0003-1600-7322

[3] Professor, National University of Sciences and Technology (Pakistan), a.shah@smme.nust.edu.pk,
ORCID iD: https://orcid.org/0000-0002-4845-9350

[4] Assistant Professor, National University of Sciences and Technology (Pakistan), mnasir@ceme.nust.edu.pk,
ORCID iD: https://orcid.org/0000-0001-9620-5980

[5] Assistant Professor, National University of Sciences and Technology (Pakistan), asif.mansure@pnec.nust.edu.pk,
ORCID iD: https://orcid.org/0000-0002-2127-0961

[6] Assistant Professor, National University of Sciences and Technology (Pakistan), abbas.hussain@pnec.nust.edu.pk,
ORCID iD: https://orcid.org/0009-0008-1680-6507

[7] Lecturer, Atlantic Technological University (Ireland), Muhammad.Ali@atu.ie,
ORCID iD: https://orcid.org/0000-0001-8236-2459

[8] Assistant Professor, Taibah University (Kingdom of Saudi Arabia), snahmed@taibahu.edu.sa,
ORCID iD: https://orcid.org/0009-0008-1680-6507

Memoria Investigaciones en Ingeniería, núm. 30 (2026). pp. 30-55
https://doi.org/10.36561/ING.30.4
ISSN 2301-1092 • ISSN (en línea) 2301-1106 – Universidad de Montevideo, Uruguay

Keywords: Finite Element Method (FEM); Goldak's double ellipsoidal model; SMAW; Solid Mechanics; Thermal distribution.

Resumen. - *La soldadura por arco metálico protegido (SMAW) se emplea ampliamente en la fabricación de acero estructural; sin embargo, la respuesta termomecánica de las uniones de aceros estructurales disímiles aún no se ha explorado suficientemente mediante modelado numérico. En este estudio, se desarrolla un modelo tridimensional transitorio termomecánico de elementos finitos para investigar la SMAW de placas de acero disímiles S355J2+N y ASTM A572 Grado 50. Se implementa la fuente de calor elipsoidal doble de Goldak para representar el aporte de calor del arco, y se emplea un diseño Box-Behnken para examinar sistemáticamente la influencia de la corriente de soldadura, el voltaje y la velocidad de avance. El análisis se centra en la temperatura máxima, la distorsión fuera del plano y los indicadores de tensión elástica derivados de una formulación termoelástica lineal. Los resultados indican que la corriente de soldadura rige predominantemente la temperatura máxima, mientras que la velocidad de avance tiene la mayor influencia en los gradientes térmicos y el comportamiento de distorsión; el voltaje exhibe un efecto secundario, pero no despreciable, en la distribución del calor. Las tendencias térmicas y de deformación simuladas se comparan con estudios experimentales y numéricos publicados sobre aceros estructurales comparables y muestran un comportamiento cualitativo consistente. Debido a la ausencia de plasticidad, propiedades del material dependientes de la temperatura y validación experimental directa, los resultados de tensión se interpretan únicamente como indicadores cualitativos, en lugar de tensiones residuales físicamente realistas. Este estudio proporciona un marco de sensibilidad termoelástico estructurado basado en el método de elementos finitos (MEF) y el diseño de experimentos para una combinación de aceros estructurales diferentes, no reportada previamente en estudios numéricos de soldadura por arco con electrodo revestido (SMAW). Esto ofrece información práctica para la selección de parámetros para el control térmico y de distorsión en la fabricación de acero estructural.*

Palabras clave: *Método de elementos finitos (MEF); Modelo elipsoidal doble de Goldak; SMAW; Mecánica de sólidos; Distribución térmica.*

***Resumo*. -** *A soldagem a arco com eletrodo revestido (SMAW) é amplamente empregada na fabricação de aço estrutural; no entanto, a resposta termomecânica de juntas de aço estrutural dissimilares permanece insuficientemente explorada por meio de modelagem numérica. Neste estudo, um modelo tridimensional transiente de elementos finitos termomecânicos é desenvolvido para investigar a soldagem a arco com eletrodo revestido de chapas de aço dissimilares S355J2+N e ASTM A572 Grau 50. A fonte de calor de duplo elipsoide de Goldak é implementada para representar a entrada de calor do arco, e um planejamento Box-Behnken é empregado para examinar sistematicamente a influência da corrente de soldagem, da tensão e da velocidade de deslocamento. A análise concentra-se na temperatura máxima, na distorção fora do plano e nos indicadores de tensão elástica derivados de uma formulação termoelástica linear. Os resultados indicam que a corrente de soldagem governa predominantemente a temperatura máxima, enquanto a velocidade de deslocamento tem a influência mais forte nos gradientes térmicos e no comportamento de distorção; a tensão apresenta um efeito secundário, mas não desprezível, na distribuição de calor. As tendências térmicas e de deformação simuladas são comparadas com estudos experimentais e numéricos publicados sobre aços estruturais comparáveis e mostram um comportamento qualitativo consistente. Devido à ausência de plasticidade, propriedades do material dependentes da temperatura e validação experimental direta, os resultados de tensão são interpretados apenas como indicadores qualitativos, em vez de tensões residuais fisicamente realistas. O estudo fornece uma estrutura de sensibilidade termoelástica baseada no método dos elementos finitos (MEF) e no planejamento de experimentos para uma combinação de aços estruturais distintos, não relatada anteriormente em estudos numéricos de soldagem com eletrodo revestido (SMAW), oferecendo informações práticas sobre a seleção de parâmetros para o controle térmico e de distorção na fabricação de aço estrutural.*

Palavras-chave: *Método dos Elementos Finitos (MEF); Modelo elipsoidal duplo de Goldak; SMAW; Mecânica dos Sólidos; Distribuição térmica.*

1. Introduction. - Welding is one of the most widely used fabrication processes for permanently joining metallic components in structural, pressure vessel, shipbuilding, and repair applications. In fusion welding processes, the joint is formed by localized melting of the base (parent) material with or without the addition of a consumable filler metal, followed by solidification to create a welded joint or weldment [1], [2]. The selection of welding consumables is typically guided by compatibility with the parent materials in order to achieve acceptable metallurgical integrity and mechanical performance of the joint.

Among conventional arc welding techniques, Shielded Metal Arc Welding (SMAW), also referred to as stick welding, remains one of the most versatile and widely adopted processes due to its simplicity, portability, and applicability in both indoor and outdoor environments. SMAW is extensively employed in construction, shipbuilding, maintenance, and repair industries. In this process, an electric arc is established between a flux-coated consumable electrode and the workpiece, generating the heat required for melting the base metal and filler material. The decomposition of the flux coating produces shielding gases and slag, which protect the molten weld pool from atmospheric contamination such as oxygen and hydrogen, thereby reducing defects such as porosity and cracking [2–4]. A schematic representation of the SMAW process and its associated heat source modeling framework is shown in Fig. 1. The figure illustrates the interaction between the welding arc, consumable electrode, base metals, and the implementation of the moving heat source within the finite element domain.

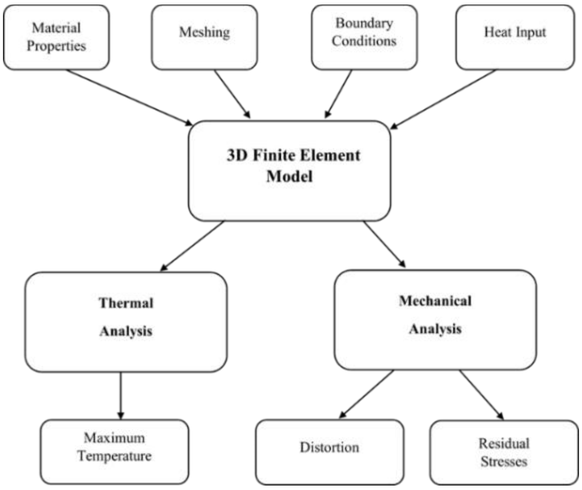

Figure I. Schematic representation of the Shielded Metal Arc Welding (SMAW) process and numerical modeling framework adopted in the present study. [4].

Despite its widespread industrial use, SMAW involves highly localized and transient thermal cycles that induce steep temperature gradients within the weldment. These thermal gradients, in turn, govern the evolution of microstructure, distortion, and residual stresses, which critically influence the dimensional accuracy and service performance of welded components. As a result, understanding the influence of welding parameters, such as current, voltage, and travel speed, on thermal and mechanical responses remains a central concern in welding science and engineering.

In recent decades, finite element modeling (FEM) has emerged as a powerful tool for analyzing welding processes, offering detailed insight into transient temperature fields, deformation behavior, and stress development that are difficult to measure experimentally. Numerous studies have investigated the effects of welding parameters on similar and dissimilar materials using both experimental and numerical approaches.

Table I summarizes representative experimental and numerical studies investigating the influence of welding parameters on thermal, mechanical, and metallurgical responses for various arc welding processes and materials [4–40].

	Author(s)	**Welding Process**	**Material**	**Findings**
1	M. E. Aalami-Aleagha et al [4]	SMAW	Steel pipe API 5L grade	Moderate Current produced optimum hardness.
2	Hunchul Jeong et al. [5]	GTAW	Aluminum A16061	reverse polarity produced more heat input than straight polarity.
3	Chao Wang et al. [6]	GMAW	SM400A	Residual stresses more with welding increased local heating and cutting.
4	Dong Ho Bae et al. [7]	GTAW	SUS304L	Longitudnal Residual Stress = 300 MPa; wider stress zones obtained with double ellipsoid model than ramp heat input model.
5	Chang-Sung Seok et al. [8]	MIG	High tensile steel H-plate	Maximum tensile residual stress found at center of thickness.
6	Chang-Sung Seok et al. [9]	GMAW	Steel Pipe	C-seam weldment on pipe produced larger longitudinal bending deformation than the L-seam pipe.
7	Dong-Yoon Kim et al. [10]	GMAW	Hot press forming steel sheets	Low Wire feed speed produced and current produced high tensile strength.
8	Yong Hua Shi et al. [11]	K-TIG	Q345	Segmentation LSTM Model has 95.2% accuracy to recognize the weld penetration state.
9	Zeng Liu et al. [12]	GMAW	High nitrogen and martensitic low alloy steel	ER 307Mo filler metal produced lower porosity and optimum joint strength as compared to ER 2209 and ER 120 S-G.
10	M. Mazar Atabaki et al. [13]	HLAW	High strength quenched and tempered steel	Stand-off distance had more impact on weld quality and penetration as compared to welding speed and power.
11	Qiang Lang et al. [14]	TIG	Transformation induced plasticity (TRIP) Steel	Addition of Laser to low current TIG increased weld depth and changed the fracture form from brittle to ductile.
12	Guoqing Wu et al. [15]	Tungsten-Argon Welding	LA141 alloy plates	With argon protection device and homogenous welding wires, the tensile strength increased to 124 MPa i.e 95% of base metal and microhardness improved.
13	A. G. Kamble et al. [16]	GMAW	AISI 321 SS plates	Bead penetration is increased with an increase in speed, gas flow rate, and wire feed rate.
14	Rohit Jha et al. [17]	TIG	MS	Maximum tensile strength at the highest current of 110 A and a welding speed of 157.80 mm/min.
15	Afnan Dadi et al. [18]	SMAW	MS SA-516 Gr. 70	Highest tensile strength obtained at a current of 120 A.
16	R. A. Mohammed et al. [19]	SMAW	Medium Carbon Steel	Highest hardness and tensile strength but lower impact strength obtained at HAZ than weldment and parent metal.
17	Brijesh Sharma et al. [20]	SMAW and GMAW	MS 2062	Maximum penetration and optimum bead obtained with SMAW, at current = 100 A, voltage = 24 V and arc length = 3mm, as compared to GMAW.
18	Asibeluo et al. [21]	SMAW	A-36 steel	Highest hardness of 114 HB was obtained at lowest current of 70 A.
19	J.O. Olawale et al [22]	SMAW	Low carbon steel	Increase in current increased the tensile strength and hardness but reduced impact strength.
20	Abhishek Shukla et al. [23]	SMAW	AISI 1020	RSM and experimental results are closer and maximum current of 120 A provided the highest tensile strength of 259 MPa.

21	Randy Chiong et al. [24]	SMAW	AISI 1018	Maximum hardness and tensile strength, 452 MPa and 195 HV, respectively, obtained at highest current.
22	Deepak Pathak et al. [25]	SMAW	Low carbon steel	Highest tensile strength observed at DCEN polarity and highest current.
23	S.H. Zoalfakar et al. [26]	SMAW	ST 37/2, ST 44/2, and ST 52/3 steel plates	Increasing Carbon equivalent (C.E) % and groove angle, increased the tensile strength and hardness.
24	Edi Widodo et al. [27]	SMAW	SS AISI 304	Highest tensile strength of 632 MPa obtained at highest current of 90 A.
25	Dhananjay Kumar et al. [28]	TIG and SMAW	SS 304L	Distortion of TIG was lesser as compared to SMAW.
26	A.K. Rude et al. [29]	SMAW	MS	Micro hardness decreases with increase in welding current but increases with number of layers.
27	Rajiv Selvam et al. [30]	SMAW	Carbon steel pipes	E- 6010 and E-7018 filler metals produced greater hardness, ductility, and toughness as compared to E-7010 and E-7018.
28	L. S. Sisira K Weerasekralage et al. [31]	SMAW	MS	Highest weldment quality obtained with current of 123 A, voltage of 27 V, and 60 º included angle.
29	Digambar Benne et al. [32]	SMAW	MS	With increase in current, voltage, and speed, the hard-faced part’s hardness and impact strength was increased.
30	Talabi et al. [33]	SMAW	Low carbon steel	Increase in current and voltage increased the tensile strength and yield strength but reduced the hardness.
31	U.S. Patil et al. [34]	SMAW	SS 304 and MS 1018	With the current = 85 A, welding speed = 8 mm/s, electrode angle of 30 º, and root gap of 0.75 mm. the highest tensile strength of 403 N/mm^2 is obtained.
32	Mahmud Khan et al.[35]	SMAW and TIG	SS AISI 304 and MS AISI 1020	TIG produced the highest tensile strength, % elongation and yield strength as compared to SMAW.
33	Mauricio Andres Rojas Nova et al. [36]	SMAW	A 36 Steel	Increase in travel speed decreases the maximum temperature. Optimum welding speed is obtained when temperature of source produces temperature just above the melting point of base metal.
34	M Matuszewski [37]	TIG and MIG	Aluminum alloy 6060 sheet	TIG with argon shielded with addition of metallic wire; MIG determined the fusion zone of sheets.
35	Sajeeb A.M. [38]	TIG	Aluminum alloy 6061-T6	Weld penetration was increased by increase in current and deacrease in stand-off distance. Current is found to be the most significant parameter.
36	A. Boudiaf et al. [39]	GTAW	AISI 316L	The highest temperature was observed at the ceneter of the source; 2D model is closer to experminetal results.
37	Cronje M [40]	SMAW	MS	Maximum distortion observed at the edge of geometry due to less heat dissipation and decreasing heat sink effect.

Table I. Examples of welding parameters' effect on Steel Specimen from Literature.

Across these studies, welding current is consistently reported as the dominant parameter governing heat input, with higher currents leading to increased peak temperatures, deeper penetration, and enhanced hardness or tensile strength in carbon and structural steels [4, 14, 18–24, 33]. Welding voltage primarily influences arc stability and bead geometry, indirectly affecting thermal distribution and residual stress development [3, 17, 20]. In contrast, welding travel speed is repeatedly shown to act as a controlling parameter for heat input density, where increased speed reduces peak temperature, limits fusion zone width, and mitigates distortion and residual stress accumulation [25, 33, 37, 40]. Several studies further highlight that excessive heat input, while improving penetration, can adversely increase distortion and tensile residual stresses, emphasizing the need for balanced parameter selection [6, 9, 28]. Despite these advances, the majority of reported investigations focus on similar material joints or experimental optimization, with comparatively fewer studies addressing three-dimensional transient thermo-mechanical modeling of dissimilar structural steel welds using systematic DOE-based sensitivity analysis.

However, a careful examination of the existing literature reveals two important gaps. First, while extensive work exists on SMAW of carbon steels, stainless steels, and aluminum alloys, numerical investigations focusing specifically on dissimilar structural steel combinations remain limited. Second, although response surface methodologies (RSM) and design of experiments (DOE) techniques have been successfully applied to welding processes, their integration with three-dimensional transient thermo-mechanical FEM for SMAW remains relatively underexplored, particularly for dissimilar steel joints.

Notably, to the best of our knowledge, no prior numerical study has reported on SMAW welding between S355J2+N and ASTM A572 Grade 50 structural steel plates, despite the widespread industrial use of both materials in load-bearing applications. These steels are commonly employed in construction and infrastructure projects, where dimensional stability and thermal distortion control are critical. Understanding the sensitivity of their thermo-mechanical response to welding parameters is therefore of practical importance.

In this study, a three-dimensional transient thermo-mechanical finite element model of the SMAW process for dissimilar S355J2+N / ASTM A572 Gr.50 steel plates is developed using COMSOL Multiphysics. Goldak's double-ellipsoidal heat source formulation is employed to represent the arc heat input. A Box–Behnken design (BBD) is adopted to systematically investigate the effects of welding current, voltage, and travel speed on key response variables, namely maximum temperature, distortion, and elastic stress indicators. Regression and analysis of variance (ANOVA) techniques are used to quantify the relative influence of process parameters and to identify dominant trends in the thermo-mechanical response.

The novelty of the present work does not lie in proposing a new welding model, but rather in providing a systematic thermo-elastic and DOE-based sensitivity assessment for a dissimilar structural steel joint that has not been previously reported in SMAW numerical studies. The results offer quantitative insight into the relative importance of welding parameters on thermal and distortion behavior, thereby providing a parameter-screening framework that can assist in distortion control and process planning for structural steel fabrication.

2. Research Methodology. –

2.1 Materials Selection and Geometry. - There are two different materials in this research for welding simulation which include S355J2+N and ASTM A572 Gr.50 structural steel plates. The filler material has been assumed to be one of the base metals i.e., S355J2+N. Table II shows the material properties and chemical composition of metals. The material properties were adopted from published literature and standard material databases commonly used in numerical welding simulations [36], [37], [40]. The thermal conductivity and specific heat capacity were adopted from the standard steel material library available in COMSOL Multiphysics and commonly used literature sources. At the same time, density values were taken from experimentally reported ranges for the selected steels. In the present study, all thermal and mechanical properties were assumed to be temperature-independent. This simplification was adopted to focus on the comparative influence of welding parameters on thermal distribution and deformation, while maintaining reasonable computational efficiency. Although temperature-dependent properties are known to influence residual stress development, their inclusion was beyond the scope of the current thermo-elastic framework.

Material	Material Properties			Chemical Composition				
	Young's Modulus (GPa)	Density ($\frac{Kg}{m^3}$)	Poison ratio	C	Mn	P	S	Si
S355J2+N	200	7700 to 8030	0.3	0.22	1.60	0.035	0.035	0.55
ASTM A572 Gr. 50	190 - 210	7800	0.27-0.30	0.23	1.35	0.030	1.03	0.40

Table II. Material Properties and Chemical Composition of Metals.

The joint geometry of the dissimilar metals is shown in Figure 2. As per ISO-9692, the joint preparation of structural steel plates was carried out on AutoCAD 2021 and 3D design was made on SolidWorks 2016.

The 2D model was designed keeping in view the recommended root gap, root face, material thickness, and bevel angle. (Figures II(a) and II(b)) shows that the geometry consists of a root gap of 3 mm, a root face of 3 mm, and an included angle of 60 °. The dimensions are given in millimeters.

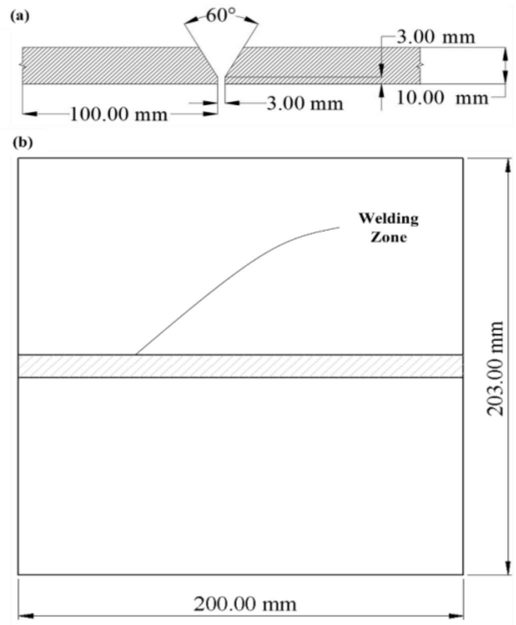

Figure II. Three-dimensional finite element model of the dissimilar S355J2+N / ASTM A572 Gr.50 butt joint used for thermo-mechanical simulation. [43]

2.2 Heat Source Modelling. - The current simulation work involves the use of Goldak's double ellipsoidal heat source model for simulating the SMAW process to provide a real-life experimental experience. This model is based on the Gaussian distribution of power density and offers versatility to both deep and shallow penetration welds. The heat source model has a steeper thermal gradient at the front and slightly steeper at the rear side of the ellipsoid [44], [45].

In cartesian coordinates, the power density distribution for the front and rear is given as follows [46]:

The distribution for the front quadrant:

$$q_f(x,y,z,t) = \frac{6\sqrt{3}f_f Q}{abc_f\pi\sqrt{\pi}} exp\left\{-3\left(\frac{x^2}{a^2}+\frac{y^2}{b^2}+\frac{(z+vt)^2}{c_f{}^2}\right)\right\} \quad [1]$$

Likewise, for the rear quadrant:

$$q_r(x, y, z, t) = \frac{6\sqrt{3} f_r Q}{abc_r\pi\sqrt{\pi}} exp\left\{-3\left(\frac{x^2}{a^2} + \frac{y^2}{b^2} + \frac{(z+vt)^2}{c_r{}^2}\right)\right\} \qquad [2]$$

where, x, y, and z are the local spatial coordinates.

$$Q = \eta V I \qquad [3]$$

where V is the Voltage (V), I is the current (A), and η is the thermal efficiency (%).

The product of the voltage (V), current (I), and thermal efficiency (η), is typically 80% for SMAW, which means that power provided by the welding source is 80% converted to the thermal energy required for welding. ν is the welding speed and t is the present time.

The f_f and f_r are the heat fraction parameters for the front and rear quadrants respectively, and their sum is equal to two. The recommended values stated by Goldak et al. (1984) are f_f = 0.6 and f_r = 1.4.

The thermal analysis of the 3D model involves the most important factor known to be the conservation of energy.

The governing equation related to transient heat transfer analysis in welding is denoted by (Equation [3]) [47].

$$\rho c \frac{\partial T}{\partial t}(x, y, z, t) = \nabla . \vec{q}(x, y, z, t) + Q\,(x, y, z, t) \qquad [4]$$

where, ρ is the density of materials ($\frac{Kg}{m^3}$), c is the specific heat capacity, T is the current temperature, $\vec{q}$ is the flux vector, Q is the internal rate of heat generation, x, y, and z are the coordinates in the reference system, and t is time.

It is assumed that there will be radiation losses from the outer surface of the plates by both, convection, and radiation. The heat losses will be prominent around and in the weldment via radiation whereas the area away from the weld zone will experience heat loss through convection [48], [49]. Hence, a combined heat transfer coefficient is used and computed from (Equation [5]) [50].

$$\tilde{h} = \frac{\varepsilon_{em}\sigma_{bol}\,((T+273)^4 - (T_{amb}+273)^4)}{(T - T_{amb})} + h_{con} \qquad [5]$$

where, $\tilde{h}$ is the combined heat transfer coefficient, ε_{em} is the emissivity σ_{bol} the Stefan Boltzmann constant, T_{amb} is the ambient temperature, and h_{con} is the convective heat transfer coefficient.

The parameters in the 3D double ellipsoidal model are given in the following Table III and the welding parameters in Table IV. Goldak's double ellipsoidal 3D heat source model is validated with the experimental results obtained by Christensen et al [50].

Parameters	**Value**	
Length of the front ellipsoid	c_f	12.9 mm
Length of the rear ellipsoid	c_r	10.3mm
Depth of penetration	b	3 mm
Width of heat source	a	8 mm
Front heat fraction	f_f	0.6
Rear heat fraction	f_r	1.4

Table III. Double ellipsoidal heat source parameters [51].

Welding Parameters	**Values**			
Arc Voltage	V	22 V	24 V	26 V
Current	I	120 A	140 A	160 A
Welding Speed	vel	3 mm/s	5 mm/s	7 mm/s
Heat Source Efficiency	η	80%		

Table IV. Welding Parameters for SMAW [39].

2.3 Design of Experiments (DOE). - The excessive current and voltage during the welding process may induce stresses and distortion in the welding geometry along with other defects. Also, the lower current and voltage settings may result in incomplete joint penetration and more spatter. Moreover, slow welding speed leads to concentrated heat input at a particular weld location which causes distortion. On the other hand, the fast-welding speed leads to incomplete weld penetration but less distortion. These effects cause weak welding strength and poor weld quality.

To cater to this issue, the process parameters require optimization either via several experiments or through a parametric numerical simulation. So, the simulation tool for analysis and optimization of SMAW process parameters is to be used. Therefore, a 3D simulation of weld geometry with modules coupled (Heat transfer with Solid Mechanics) in COMSOL Multiphysics 5.5 simulation software is built for the present study.

The Box-Behnken Design (BBD) is a form of response surface methodology (RSM) that requires at least three levels to run a single experiment. In this study, the three-level-three-factor BBD technique was applied to obtain the best combination of welding variables for the sound quality of the weld [52], [53], [54], [55], [56]. Table V represents the chosen welding variables along with their levels.

Order No.	**LEVELS USING BBD**			**ACTUAL VALUES**		
	V	I	vel	V	I	vel
	-1	-1	0	22	120	0.005
	-1	1	0	22	160	0.005
	1	-1	0	26	120	0.005
	1	1	0	26	160	0.005
	-1	0	-1	22	140	0.003
	-1	0	1	22	140	0.007
	1	0	-1	26	140	0.003
	1	0	1	26	140	0.007
	0	-1	-1	24	120	0.003
	0	-1	1	24	120	0.007
	0	1	-1	24	160	0.003
	0	1	1	24	160	0.007
	0	0	0	24	140	0.005
	0	0	0	24	140	0.005
	0	0	0	24	140	0.005

Table V. Assigning Levels to the Process Parameters.

There are three levels i.e., -1, 0, and 1 for each parameter which corresponds to the lowest level, central level, and the highest level of parameter values. Table V shows 15 different combinations of input process parameters with the levels assigned and the actual values of the input parameters.

2.4 Simulation Procedure. - The 3D graphical model of the welded joint was developed in SOLIDWORKS 2016 and imported into COMSOL Multiphysics 5.5 for the thermo-mechanical simulation of the SMAW process. The geometry consists of two steel plates (S355J2+N and ASTM A572 Gr.50) and a central weld region configured as a Single-V groove butt joint, following ISO-9692 recommendations for joint preparation [43].

The Heat Transfer in Solids and Solid Mechanics physics interfaces were applied in a coupled manner to capture both the transient thermal response and the resulting elastic deformation. Goldak's double-ellipsoidal heat source formulation was implemented according to the procedure described in [44–46], and the associated welding parameters are summarized in Table VI. The initial temperature was set at 25 °C, and heat losses from external surfaces were treated using convection and radiation boundary conditions based on the methodology described in [48–50]. The total heat input was calculated using the arc efficiency for SMAW reported in [51].

Parameter	**Value**	**Description**
x0	-0.10 m	Heat source center x-coordinate
y0	0 m	Heat source center y-coordinate
z0	-0.002 m	Heat source center z-coordinate
vel	0.003 m/s	Welding speed
V	22 V	Welding voltage
I	120 A	Welding current
u	0.8	Weld efficiency
af	0.0129 m	Length of front ellipsoidal
ar	0.0103 m	Length of rear ellipsoidal
b	0.003 m	Depth of penetration
c	0.005 m	Width of heat source
Ff	0.6	Heat fraction (front)
Fr	1.4	Heat fraction (rear)
cf	0.0129 m	Front length of the weld pool
cr	0.0103 m	Rear length of the weld pool
Q	3200	Heat input

a	0.008 m	Weld width/2
q01	1.1574 x 10^{10}	Power density Distribution for the front part
q02	3.3823 x 10^{10}	Power density distribution for the rear part
p	1.0133 x 10^{8} Pa	Pressure

Table VI. Defining the parameters for the 3D geometry.

The resulting transient temperature field was then used as a thermal load in the structural analysis. All materials were modelled as linear elastic, consistent with the simplified thermo-elastic welding models commonly reported in earlier studies [57], [58]. Temperature-dependent mechanical properties, plasticity, creep, and phase transformation effects were not included, and therefore the mechanical results represent elastic strain-based indicators of deformation rather than true physical residual stress magnitudes. Accordingly, the von Mises stress values are interpreted only for comparative analysis between welding conditions, not as actual residual stresses.

A free boundary condition was applied to allow unconstrained deformation of the plates. No external clamps or fixtures were used. The absence of mechanical constraints allows free distortion and therefore represents an upper-bound estimate of deformation, while constrained welding conditions would be expected to reduce out-of-plane displacement but increase residual stresses.

The simulation was run as a time-dependent study from 0 to 67 s, corresponding to the weld-travel time at 0.003 m/s, while higher speeds (0.005 and 0.007 m/s) reduced the welding duration to approximately 40 s.

The mesh was generated using physics-controlled tetrahedral elements, with refinement along the weld line to capture steep thermal gradients. This meshing strategy follows recommendations in prior finite element welding simulations [36], [37], [40]. Figure 3 shows the final meshed geometry.

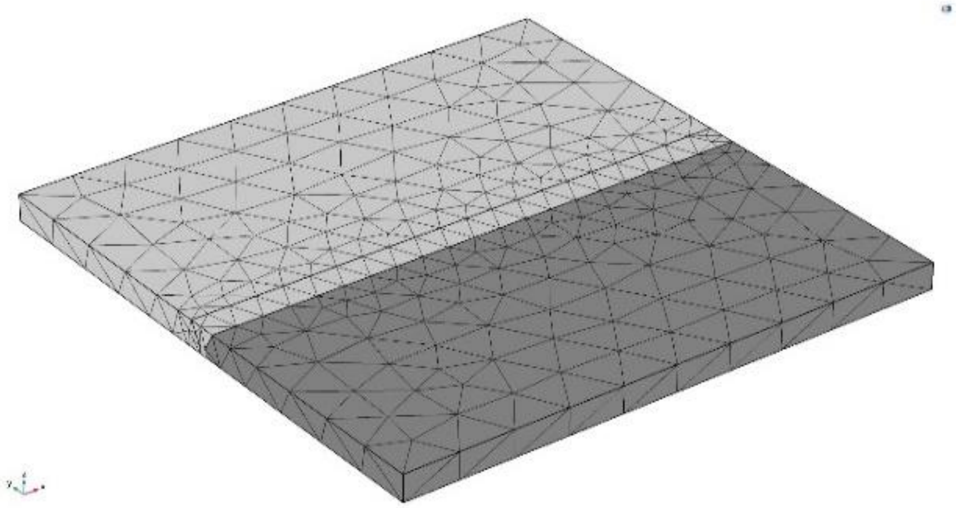

Figure III. Meshing strategy employed for the SMAW numerical model

In this study, the simulation time range was set from 0 to 67 s with a time step of 0.05 s. At a welding speed of 0.003 m/s, the 200 mm weld length requires approximately 67 s for completion in a single pass. At higher speeds of 0.005 m/s and 0.007 m/s, the same weld length is completed in approximately 40 s.

2.5 Temperature Profiles. - Figure 4 illustrates the evolution of the temperature field as the Goldak double-ellipsoidal heat source moves along the weld line in the x-direction. Welding begins from the left-hand side of the joint, and the transient temperature contours at four representative times (t = 15 s, 25 s, 30 s, and 35 s) are shown in Figures 4(a–d). The highest temperatures occur in the weld pool and the immediate heat-affected zone, while temperatures decrease rapidly away from the heat source due to conduction and surface heat losses.

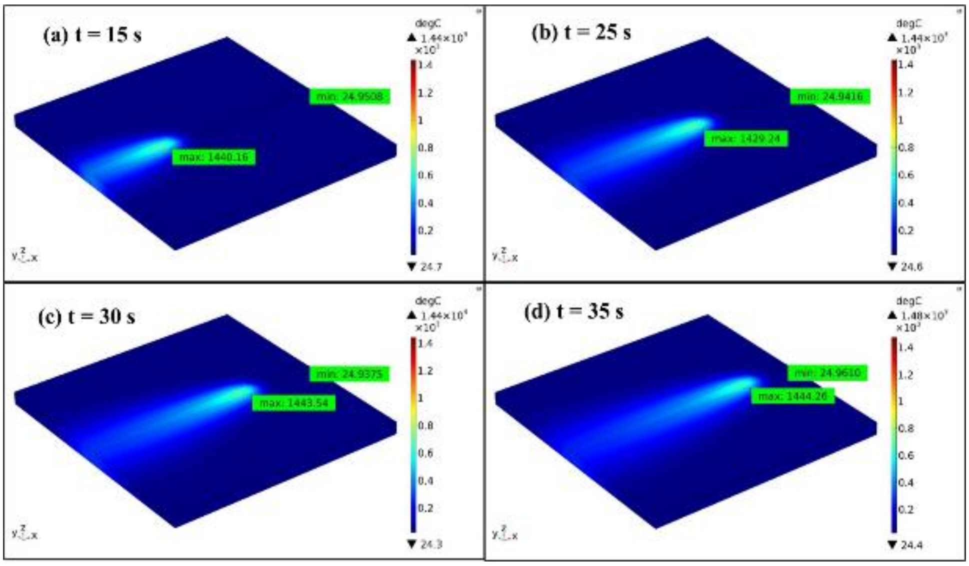

Figure IV. Goldak double-ellipsoidal heat source representation used to model arc heat input in the SMAW process (a) t = 15s, (b) t = 25s, (c) t = 30s, (d) t =35s.

Figures 5(a) and 5(b) present the temperature distribution along the depth (z-axis) and the transverse direction (y-axis), respectively. As expected, the temperature decreases with depth below the weld centerline and laterally across the plate thickness. Once the local temperature exceeds approximately 1425 °C, melting initiates, and the weld metal begins to form the fusion bond at the joint interface.

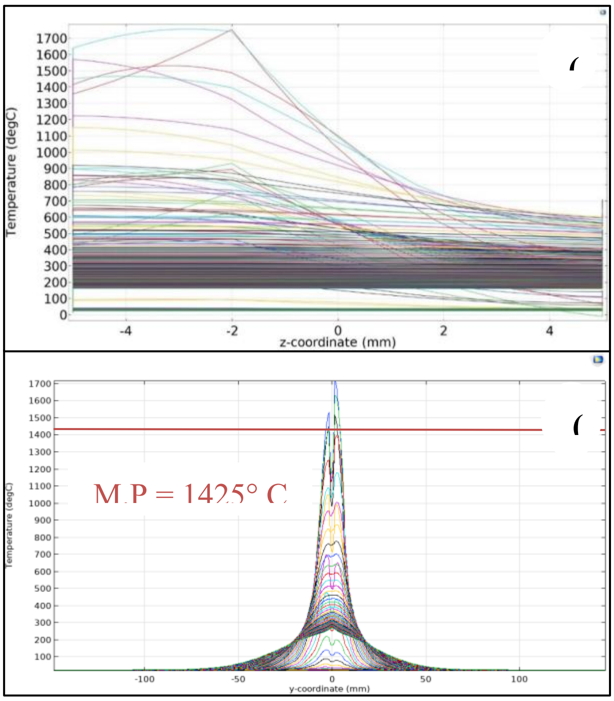

Figure V. Transient temperature distribution. (a)Temperature vs Z-coordinate, and (b) Temperature vs Y-coordinates.

2.6 Structural Stresses and Deformation. - Figures 6(a) and 6(b) present the elastic von Mises stress indicator obtained from the thermo-elastic structural model. As noted earlier, the mechanical analysis was performed using linear-elastic material behaviour; therefore, the reported von Mises values represent qualitative elastic stress indicators rather than physical residual stress magnitudes. These indicators highlight regions where the thermal cycle generates high elastic strain and provide insight into the relative stress distribution during and immediately after welding.

Elevated elastic stress indicators appear near the weld centerline, where the material experiences the largest thermal gradients and volumetric expansion. Away from the weld pool, the indicator decreases rapidly as the temperature field becomes more uniform. Along the transverse (y-axis) direction, the maximum indicator occurs near the weld centerline, while along the longitudinal (x-axis) direction the distribution varies with the non-uniform heat input and the progression of the heat source. These trends are shown in Figures 7(a) and 7(b).

The deformation field resulting from thermal expansion and subsequent cooling is shown in Figures 8(a–c). The predicted distortion reflects the accumulated elastic strains, with maximum displacement occurring near the edges and corners of the welded plates. The Z-component displacement illustrates upward bending near the weld region, which is consistent with typical distortion behavior in butt-welded joints subjected to steep temperature gradients.

These qualitative results demonstrate how variations in heat input influence the overall deformation pattern. While quantitative residual stress predictions require elastic–plastic, temperature-dependent modelling, the present thermo-elastic simulation provides useful comparative insight into the effect of welding parameters on the distribution and magnitude of elastic strain and distortion.

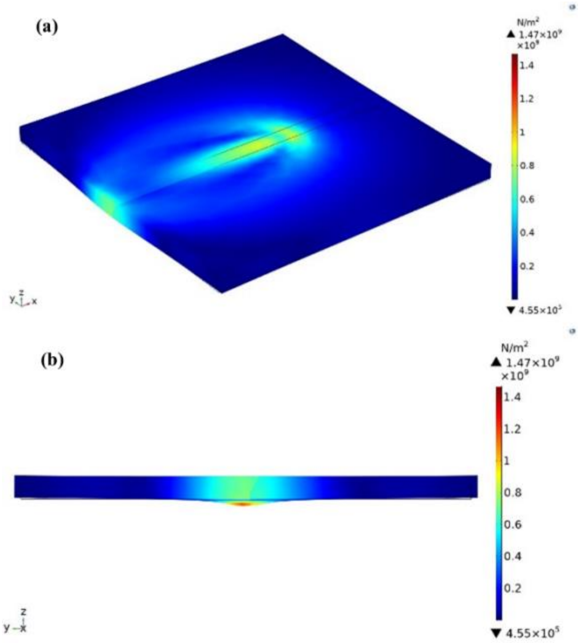

Figure VI. Elastic von Mises stress indicator distribution obtained from the linear thermo-elastic structural model at V = 24 V, I = 150 A, and welding speed = 0.004 m/s at t = 14 s: (a) y–z plane section through the weld centerline; (b) isometric view. The plotted values represent qualitative elastic stress indicators and do not correspond to true residual stresses.

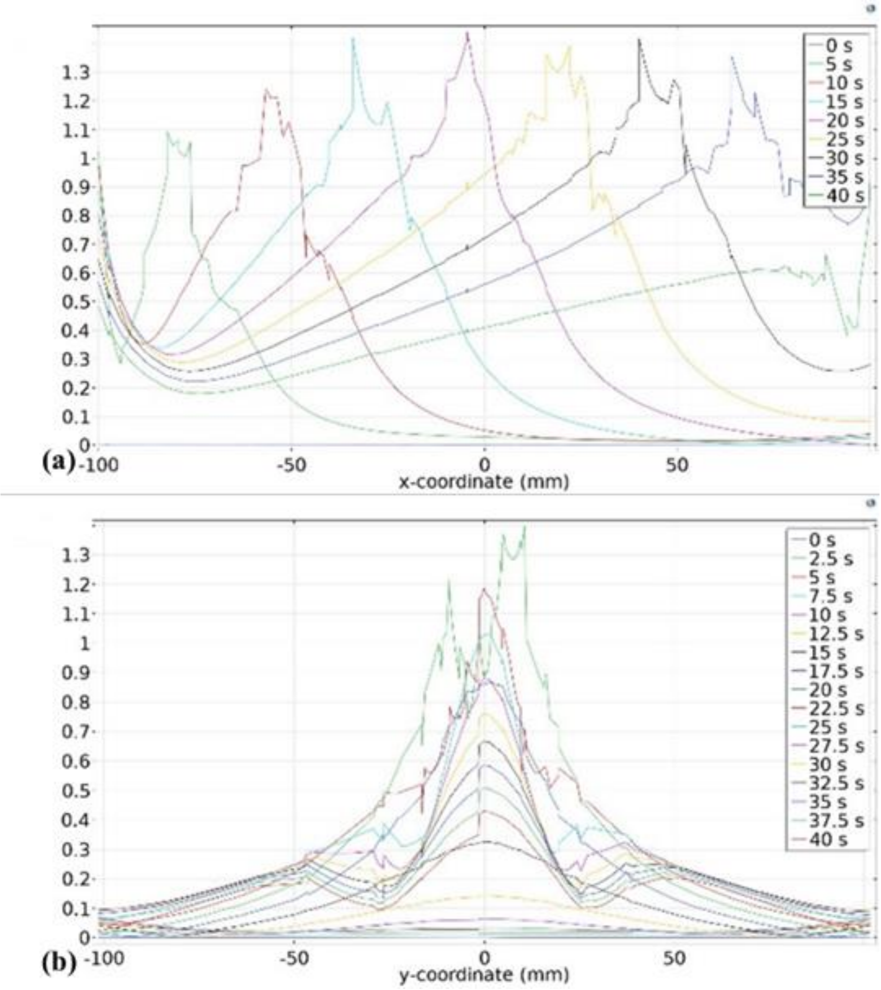

Figure VII. Distribution of the elastic von Mises indicator along (a) the longitudinal (x) direction and (b) the transverse (y) direction relative to the weld centerline.

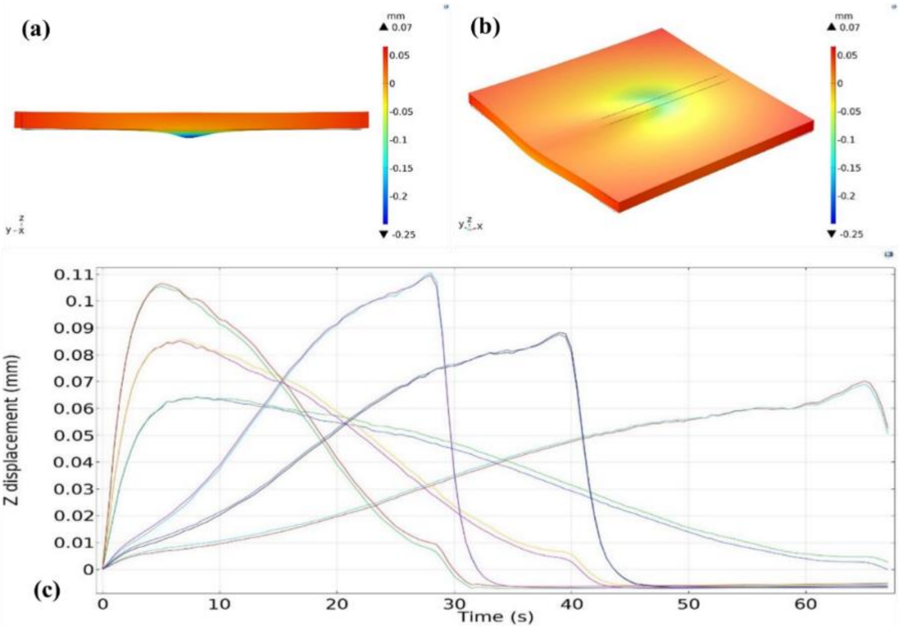

Figure VIII. Predicted displacement field from transient thermal loading: (a) global displacement magnitude, (b) isometric view of deformation, (c) Z-component displacement illustrating out-of-plane distortion after cooling.

3. Results and Discussion. -

3.1 Design of Experiments and Statistical Modelling. - A Box–Behnken Design (BBD) with three factors and three levels was employed to evaluate the influence of welding voltage, current, and welding speed on the thermo–mechanical responses of the welded joint. Multiple regression analysis was conducted following the procedures described in [59], using the response data summarized in Table VII.

Because the structural model was linear-elastic, the von Mises output (Res_Str) represents an elastic stress indicator rather than a physical residual stress. Therefore, quantitative regression and ANOVA were performed only for the physically meaningful responses, namely the Z-displacement (Td) and the maximum temperature (T_max). The elastic stress indicator (Res_Str) is retained in Table VII for qualitative comparison only and was not used to develop empirical equations.

A general parametric relationship of the form presented below was fitted to the log-transformed data for Td and T_max:.

$$Y_i = b_{0i} + b_{1i}X_1 + b_{2i}X_2 + b_{3i}X_3 \qquad [6]$$

where Y_i corresponds to log(Td) or log(T_max), $X_1 = log(V)$, $X_2 = log(I)$, and $X_3 = log(vel)$.

A log-linear model of the form shown in Equation [6] was fitted to log-transformed responses, where the predictors correspond to log(V), log(I), and log(vel). The regression coefficients were estimated using Microsoft Excel based on the approach in [59].

Order No.	Levels Defined			Actual Values			Response Parameters		
	V	I	vel	V	I	vel	Res_Str (GPa)	Td (mm)	T_max (°C)
1	-1	-1	0	22	120	0.005	3.581E+09	0.0679	1090.2
2	-1	1	0	22	160	0.005	4.638E+09	0.0939	1585
3	1	-1	0	26	120	0.005	3.122E+09	0.0805	1334.9
4	1	1	0	26	160	0.005	1.468E+09	0.0486	2506.5
5	-1	0	-1	22	140	0.003	1.722E+09	0.062	2538.8
6	-1	0	1	22	140	0.007	1.13E+09	0.0573	1924.7
7	1	0	-1	26	140	0.003	1.679E+09	0.0555	3044.9
8	1	0	1	26	140	0.007	5.578E+09	0.0942	1500.8
9	0	-1	-1	24	120	0.003	2.32E+09	0.07	1994.7
10	0	-1	1	24	120	0.007	3.094E+09	0.0738	1103.7
11	0	1	-1	24	160	0.003	2.702E+09	0.0544	3494.1
12	0	1	1	24	160	0.007	3.315E+09	0.0992	1618.6
13	0	0	0	24	140	0.005	5.912E+09	0.0885	1488.2
14	0	0	0	24	140	0.005	5.912E+09	0.0884	1483.1
15	0	0	0	24	140	0.005	5.912E+09	0.0894	1489.3

Table VII. BBD Design and Output response values of Residual Stress (Res_Str), Displacement (Td), and Maximum Temperature (T_max)

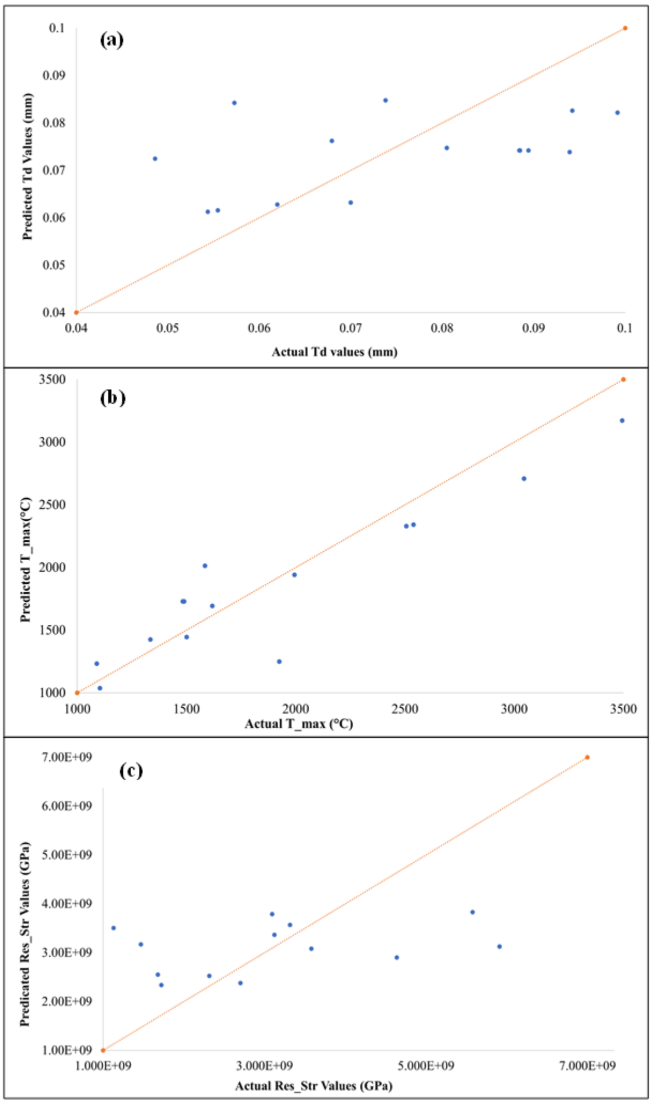

Figure IX. Scatter plots comparing actual and predicted responses for (a) distortion (Td) and (b) maximum temperature (T_max) based on log-linear regression models. The elastic stress indicator (Res_Str) is shown for completeness but was not used for regression analysis.

The regression results are summarized in Table VIII. The scatter plots of actual versus predicted values for Td and T_max are shown in Figures 9(a–b), demonstrating reasonable agreement between the predicted and observed responses, consistent with the use of log-transformed linear models [61–64].

	log Res_Str		log Td		log T_max	
Source	F-value	p-value	F-value	p-value	F-value	p-value
Model	0.3441	0.0535	1.1130	0.9738	13.0007	0.0477
log V	-	0.8352	-	0.9072	-	0.2897
log I	-	0.8879	-	0.8514	-	0.0031
log vel	-	0.3467	-	0.0971	-	0.0005
R-sq	0.0858		0.2328		0.7800	
R-sq (adj)	-0.1635		0.0236		0.7200	

Table VIII. ANOVA results for log Res_Str, log Td, and log T_max

The low R^2 value for Td indicates that a first-order log-linear model is insufficient to fully capture deformation behaviour, which is influenced by geometric stiffness and boundary effects beyond primary process parameters. The ANOVA results indicate that welding current exhibits the strongest statistical influence on T_max, as evidenced by the lowest p-value, followed by welding speed and voltage. For Td, the p-values are comparatively higher, indicating weaker explanatory power. This aligns with the sensitivity considerations described widely in welding DOE literature [65–69], in which T_max is generally more sensitive to heat-input variations than displacement.

Because Res_Str is an elastic indicator and not a physical residual stress, no empirical equation or sensitivity expression is provided for that quantity.

A formal optimization or multi-objective decision-making procedure was not performed; therefore, the results are interpreted as parametric trends rather than optimized welding conditions.

3.2 Thermal Response. - Figures 10(a) and 10(b) illustrate the maximum temperature variation along the weld line (x-axis) and through the depth (z-axis). The temperature rises rapidly once the arc initiates, reaches a peak sufficient for melting and fusion, and fluctuates slightly along the x-direction due to the evolving heat-sink effect of the surrounding base metal. Along the z-axis, the temperature decreases with depth as heat is conducted away from the active fusion zone. These thermal cycles govern melting, fusion, and the subsequent development of distortion.

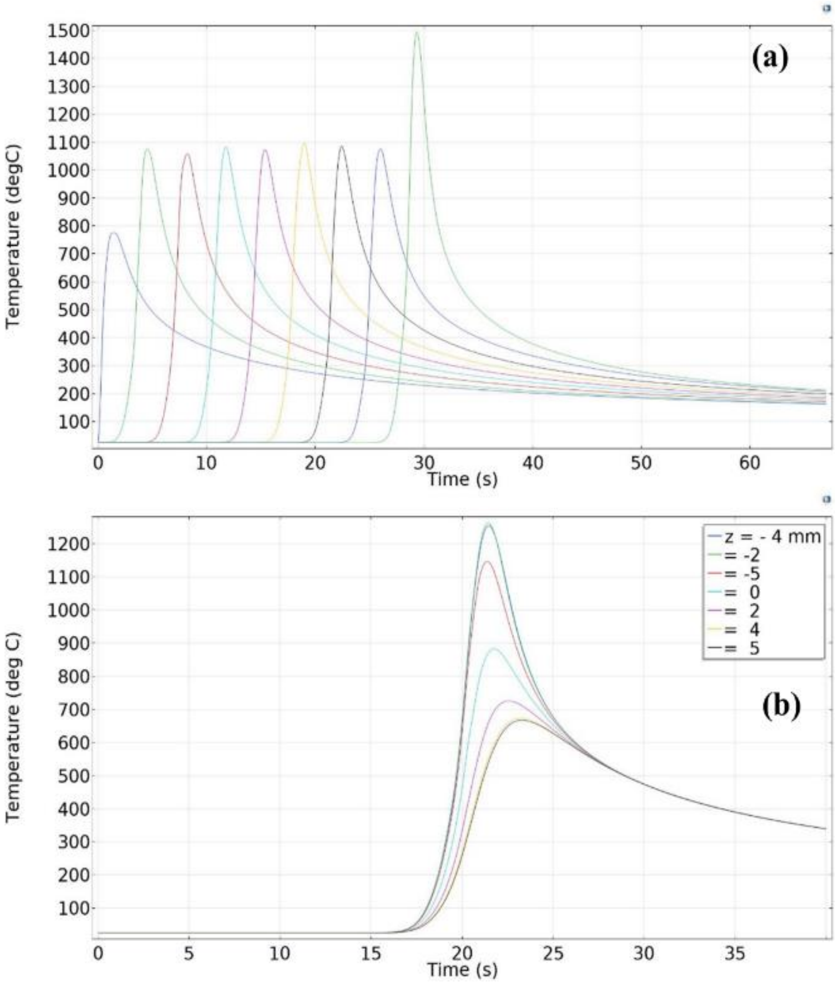

Figure X. Variation of maximum temperature (T_max) along (a) the weld line (x-axis) and (b) through the plate thickness (z-axis) during welding.

The thermal expansion and contraction associated with the heating and cooling cycle induce elastic strain fields, which are represented by the elastic von Mises indicator (Res_Str). As discussed earlier, this quantity does not represent true residual stress but provides a qualitative map of regions experiencing higher thermo-elastic loading during welding. Distortion (Td) reflects the cumulative effect of these elastic strains and the steep temperature gradients in the joint. Minimizing weld volume, optimizing heat input, and controlling inter-pass timing are common methods for reducing distortion in welded joints, as reported in previous studies [70], [71]. These general concepts are consistent with the qualitative trends observed in the present thermo-elastic model.

3.3 Heat Source benchmarking. - The Goldak double-ellipsoidal volumetric heat source implemented in this study was benchmarked by examining the thermal field behaviour, fusion-zone dimensions, and the temperature-time response at points adjacent to the weld line. The objective was to ensure that the implemented heat input parameters reproduced the characteristic features of SMAW thermal behaviour reported in the literature.

Figure IV shows the transient thermal distribution as the heat source travels along the weld line. The predicted peak temperatures exceed the melting range of the steel (~1425–1500 °C), followed by rapid cooling once the heat source moves forward. This behaviour is consistent with established SMAW thermal cycles, where peak temperatures remain concentrated in the fusion zone and decrease sharply within a few millimeters of the weld centreline [44–46], [48–50].

The predicted fusion-zone width and depth estimated from the isotherms near the melting temperature agree in magnitude with typical SMAW fusion zones reported for similar heat inputs and plate thicknesses in earlier numerical and experimental studies [36], [40], [57]. The predicted fusion zone depth of ~3 mm falls within the 2.5–3.5 mm range reported by Goldak et al.[50] for comparable SMAW heat inputs.Although the present model does not include phase transformations, the overall size and shape of the molten region fall within expected ranges for comparable voltage, current, and travel speed combinations.

The temperature–time history extracted along the weld line (Figure 11(a)) demonstrates the expected progression from rapid heating to steep cooling. The temperature fluctuations along the x-direction, including the lower temperature observed immediately at arc initiation and the slight peak towards the end of the weld, are characteristic of Goldak-type heat input profiles and reflect the evolving heat-sink conditions of the surrounding base metal. The temperature variation through the depth (Figure 11(b)) shows decreasing temperature with increasing depth, as documented in earlier SMAW simulations [47], [48].

Overall, the shape of the fusion zone, the magnitude and gradient of peak temperatures, and the transient behaviour of the temperature field confirm that the implemented Goldak heat source is physically consistent and aligns well with previously published numerical welding models.

3.4 Discussion. - The thermo–mechanical simulations performed in this study provide a clear understanding of how SMAW process parameters influence the thermal field, elastic strain distribution, and deformation in a Single-V butt joint configuration. The predicted temperature distribution is consistent with the behaviour expected from a Goldak double-ellipsoidal heat source, where the highest temperatures occur near the weld pool and rapidly decrease away from the fusion zone due to conduction and surface heat losses. The thermal gradients observed in Figures 4 and 5 follow the characteristic pattern reported in earlier numerical welding studies [44–46], [48–50], confirming correct representation of heat input and boundary conditions.

The thermal results further show that welding current and welding speed significantly influence peak temperature levels (T_max). Higher current increases heat input per unit length, resulting in a wider and deeper fusion zone, whereas higher speed reduces the time available for heat accumulation, thereby decreasing T_max. These parametric trends are consistent with SMAW physics and with previous findings in the literature [36], [40], [57]. The temperature evolution along the weld line and through the depth (Figure 11) confirms that the weld pool experiences a rapid heating phase, followed by accelerated cooling once the heat source moves forward. This behaviour governs the molten pool development and the subsequent formation of the fusion zone.

The elastic von Mises indicator (Res_Str) provides qualitative insight into regions experiencing high thermo-elastic loading during and immediately after welding. As expected, the highest elastic indicator values appear near the weld centreline, where steep thermal gradients induce differential expansion. Although these values do not represent true residual stresses due to the absence of plasticity in the structural model, the spatial trends in Figures 6 and 7 help identify zones with the greatest deformation potential. Similar qualitative stress–distribution patterns have been reported in simplified thermo-elastic welding simulations [57], [58].

The deformation results reveal that the dominant distortion mode is out-of-plane bending (Z-displacement), with peak deflection occurring near the plate edges and corners (Figures 8(a–c)). This is consistent with classical distortion mechanisms associated with butt welding, where asymmetric heating causes upward bending due to non-uniform expansion and contraction. The magnitude and distribution of Td are strongly influenced by heat input, aligning with the behaviour noted in prior experimental and numerical work [65–69].

The DOE and regression analysis provide further insight into parameter influence. The ANOVA results (Table VIII) show that welding current exerts the strongest statistical effect on T_max, followed by welding speed, while Td exhibits comparatively weak sensitivity to all three parameters. This behaviour reflects the dual dependence of distortion on both thermal gradients and the structural stiffness of the plates. The relatively low R^2 values for Td also indicate that deformation is influenced by geometric effects beyond the primary welding parameters, a trend also observed in earlier welding DOEs [62–64].

Although direct experimental validation for the S355J2+N / ASTM A572 Gr.50 joint was not available, the simulated trends, namely the increase of peak temperature with welding current and its reduction with increasing welding speed, are consistent with experimental and numerical observations reported for comparable arc-welded structural steels in the literature [21, 22, 29]. Furthermore, the predicted distortion magnitudes fall within the ranges reported for butt-welded steel plates subjected to similar heat inputs and boundary conditions [24–26].

Overall, the present simulation framework successfully captures the key qualitative relationships between welding parameters, thermal fields, and deformation. While the thermo-elastic model does not produce quantitative residual stress values, it provides reliable comparative trends that can guide parameter selection for reducing distortion. Incorporating temperature-dependent elastoplastic properties and phase transformation effects in future work will enable accurate prediction of residual stress magnitudes and allow for full validation against experimental data.

3.5 Significance of the Study. - This study provides an integrated thermo–mechanical and design-of-experiments assessment of the SMAW process for a Single-V butt joint of S355J2+N and ASTM A572 Gr.50 steels. By combining a transient Goldak-type heat source model with thermo-elastic structural analysis and a Box–Behnken design, the work establishes a coherent framework for understanding how voltage, current, and welding speed influence weld-pool thermal cycles and distortion. The results clarify the dominant role of welding current in controlling peak temperatures and demonstrate how increases in welding speed can effectively reduce thermal accumulation and limit out-of-plane deformation.

Although the structural model is elastic and therefore does not predict true residual stress magnitudes, the elastic von Mises indicator provides valuable qualitative insight into regions experiencing elevated thermo-elastic loading. This enables identification of distortion-prone zones and supports the interpretation of deformation mechanisms without requiring a full elastoplastic formulation.

The combined simulation–DOE approach offers a practical methodology for parameter screening in welded structures where distortion control is critical. The insights derived here can guide the selection of welding parameters for reducing deformation in industrial fabrication settings. Moreover, the modelling structure developed in this work provides a foundation for future enhancements involving temperature-dependent elastoplastic laws, phase-transformation effects, and experimental validation. These extensions will further strengthen the predictive capability of numerical welding simulations and contribute to optimized process planning in structural steel applications.

4. Conclusion and Future Work. - A three-dimensional transient thermo-mechanical finite element framework was developed to investigate the influence of SMAW process parameters on the thermal and deformation behavior of dissimilar S355J2+N and ASTM A572 Grade 50 steel plates. Based on the numerical simulations and parametric analysis, the following conclusions can be drawn:

1. Welding current is the dominant parameter governing peak temperature, producing a strong increase in maximum thermal response with increasing current, whereas travel speed significantly moderates thermal gradients by controlling heat input per unit length.

2. Travel speed exerts the strongest influence on out-of-plane distortion, indicating its critical role in deformation control during SMAW of structural steel joints. Voltage shows a secondary effect on both thermal distribution and deformation behavior.

3. Elastic stress fields obtained from the linear thermo-elastic analysis reveal spatial stress localization associated with thermal gradients; however, due to the absence of plasticity, stress relaxation, and temperature-dependent material properties, these results are interpreted solely as qualitative elastic stress indicators rather than physically realistic residual stresses.

4. Regression and ANOVA analyses support the qualitative identification of dominant parameters for peak temperature and distortion; nevertheless, low coefficients of determination for certain responses indicate the limitations of first-order models and restrict their use to trend interpretation rather than prediction or optimization.

5. Benchmark comparisons with published experimental and numerical studies on comparable structural steels demonstrate consistency in thermal and deformation trends, supporting the credibility of the numerical framework within its stated scope.

The primary contribution of this work lies in providing a transparent thermo-elastic FEM and design-of-experiments–based sensitivity assessment for a dissimilar structural steel combination not previously reported in SMAW numerical studies. The limitations associated with the material model and the absence of direct experimental validation are explicitly acknowledged. Future work will focus on incorporating temperature-dependent material behavior, plasticity, and experimental measurements to enable physically realistic residual stress prediction and quantitative model validation.

Future research will extend the present numerical framework by incorporating temperature-dependent thermo-physical and mechanical material properties, as well as elastic–plastic constitutive behavior, to enable physically realistic prediction of residual stresses and permanent deformation. The inclusion of phase transformation effects and stress relaxation mechanisms will further improve the fidelity of the mechanical response during heating and cooling cycles. Experimental measurements of temperature histories, fusion zone geometry, and distortion for the S355J2+N / ASTM A572 Gr.50 joint will be pursued to provide direct quantitative validation of the numerical model. In addition, refined response surface models incorporating higher-order and interaction terms, combined with formal multi-response optimization techniques, will be employed to support predictive parameter selection and process optimization. These extensions will allow the framework developed in the present study to evolve from qualitative parameter screening toward quantitatively validated welding process design.

Declaration Conflict of Interest. - The authors of this research announce that they have no known contending monetary interests or individual connections that may have impacted the work detailed in this paper.

Data and Code Availability. - Data and code shall be made available upon request to the corresponding author.

Nomenclature. –

SMAW	Shielded Metal Arc Welding
FEM	Finite Element Method
HAZ	Heat Affected Zone
C	Carbon
Si	Silicon
Mn	Manganese
vel	Welding Speed
V	Voltage
I	Current
ρ	Density of materials
c	Specific heat capacity
T	Present temperature
$\vec{q}$	Flux vector
Q	Internal rate of heat generation
x, y, z	Coordinates in the reference system
t	Time
$\tilde{h}$	Combined heat transfer coefficient
ε_{em}	Emissivity
σ_{bol}	Stefan Boltzmann Constant
T_{amb}	Ambient temperature
h_{con}	Convective heat transfer Coefficient.
η	Thermal Efficiency
c_f	Length of the front ellipsoid
GMAW	Gas Metal Arc Welding
BBD	Box-Behnken Design
RSM	Response Surface Methodology
c_r	Length of the rear ellipsoid
a	Width of heat source
b	Depth of Penetration
f_f	Front heat fraction
MS	Mild Steel
f_r	Rear heat fraction
HB	Hardness Brinell
PWHT	Post-Weld Heat Treatment
DCEN	Direct Current Electrode Negative
DCEP	Direct Current Electrode Positive
AISI	American Iron and Steel Institute
ASTM	American Society for Testing and Materials
UTS	Ultimate Tensile Strength
EL%	Percentage Elongation
TIG	Tungsten Inert Gas
GTAW	Gas Tungsten Arc Welding
LPG	Liquefied Petroleum Gas
G	Groove
F	Fillet
SS	Stainless Steel
S355	Structural Steel with a minimum yield strength of minimum 355 MP

References

[1] “What is Welding? - Definition, Processes and Types of Welds - TWI.” Accessed: Oct. 28, 2022. [Online]. Available: https://www.twi-global.com/technical-knowledge/faqs/what-is-welding

[2] “Shielded Metal Arc Welding (SMAW) [SubsTech].” Accessed: Jan. 03, 2023. [Online]. Available: https://www.substech.com/dokuwiki/doku.php?id=shielded_metal_arc_welding_smaw

[3] N. M. Kohlhorst, K. M. Faraone, R. G. Miller, G. Muralidharan, G. B. Ulrich, and J. C. Zhao, “A Technique for the Quantitative Characterization of Weld Microstructure and Application to Mo Welds,” Metallurgical and Materials Transactions B: Process Metallurgy and Materials Processing Science, vol. 54, no. 3, pp. 1434–1448, Jun. 2023, doi: 10.1007/S11663-023-02771-Y/METRICS.

[4] M. E. Aalami-Aleagha and A. M. Rashidi, “Correlated macrostructural parameters of weld and weld current in the SMAW of small pipes,” Journal of Mechanical Science and Technology, vol. 26, no. 1, pp. 181–185, 2012, doi: 10.1007/s12206-011-0939-1.

[5] H. Jeong, K. Park, and J. Cho, “Numerical analysis of variable polarity arc weld pool,” Journal of Mechanical Science and Technology, vol. 30, no. 9, pp. 4307–4313, 2016, doi: 10.1007/s12206-016-0845-7.

[6] C. Wang and J. W. Kim, “Numerical analysis of distortions by using an incorporated model for welding-heating-cutting processes of a welded lifting lug,” Journal of Mechanical Science and Technology, vol. 32, no. 12, pp. 5855–5862, 2018, doi: 10.1007/s12206-018-1134-4.

[7] D. H. Bae, C. H. Kim, S. Y. Cho, J. K. Hong, and C. L. Tsai, “Numerical analysis of welding residual stress using heat source models for the multi-pass weldment,” KSME International Journal, vol. 16, no. 9, pp. 1054–1064, 2002, doi: 10.1007/BF02984424.

[8] C. S. Seok, M. W. Suh, and J. H. Park, “Investigation of welding residual stress of high tensile steel by finite element method and experiment,” KSME International Journal, vol. 13, no. 12, pp. 879–885, 1999, doi: 10.1007/BF03184755.

[9] C. Wu, C. Lee, and J. W. Kim, “Numerical simulation of bending deformation induced by multi-seam welding of a steel-pipe structure,” Journal of Mechanical Science and Technology, vol. 34, no. 5, pp. 2121–2131, 2020, doi: 10.1007/s12206-020-0433-8.

[10] D. Y. Kim, T. H. Lee, C. Kim, M. Kang, and J. Park, “Gas metal arc welding with undermatched filler wire for hot-press-formed steel of 2.0 GPa strength: Influence of filler wire strength and bead geometry,” Mater Today Commun, vol. 34, no. December 2022, 2023, doi: 10.1016/j.mtcomm.2022.105244.

[11] Y. H. Shi, Z. S. Wang, X. Y. Chen, Y. X. Cui, T. Xu, and J. Y. Wang, “Real-time K-TIG welding penetration prediction on embedded system using a segmentation-LSTM model,” Adv Manuf, 2023, doi: 10.1007/s40436-023-00437-1.

[12] Z. Liu et al., “Investigation of the weldability of dissimilar joint between high nitrogen steel and low alloy steel by comparing filler metals,” Mater Today Commun, vol. 35, no. 92, p. 105551, 2023, doi: 10.1016/j.mtcomm.2023.105551.

[13] M. Mazar Atabaki, N. Yazdian, and R. Kovacevic, “Hybrid laser/arc welding of thick high-strength steel in different configurations,” Adv Manuf, vol. 6, no. 2, pp. 176–188, 2018, doi: 10.1007/s40436-017-0193-6.

[14] Q. Lang, X. Zhang, G. Song, and L. Liu, “Effects of different laser power and welding speed on the microstructure and mechanical properties of TRIP joints in laser-TIG arc hybrid lap filler wire welding,” Mater Today Commun, vol. 29, no. July, p. 102925, 2021, doi: 10.1016/j.mtcomm.2021.102925.

[15] G. Wu, D. Zhao, and L. Sun, “Microstructure and mechanical properties of wire-filled tungsten argon arc welded joints for LA141 magnesium-lithium-aluminum alloy,” Mater Today Commun, vol. 23, no. December 2019, p. 100881, 2020, doi: 10.1016/j.mtcomm.2019.100881.

[16] A. G. Kamble and R. V. Rao, “Experimental investigation on the effects of process parameters of GMAW and transient thermal analysis of AISI321 steel,” Adv Manuf, vol. 1, no. 4, pp. 362–377, 2013, doi: 10.1007/s40436-013-0041-2.

[17] A. K. J. Rohit Jha, “Influence of Welding Current and Joint Design on the Tensile Properties of SMAW Welded Mild Steel Joints,” International Journal of Engineering Research and Application, vol. 4, no. 6, pp. 106–111, 2014.

[18] A. Dadi, P. B. Goyal, and H. Patel, “A Review Paper on 'Optimization of Shielded Metal Arc Welding Parameters for Welding of (Ms) Sa-516 Gr . 70 Plate by Using Taguchi Approach",” Int J Sci Res Sci Technol, vol. 4, no. 5, pp. 1536–1543, 2018.

[19] R. A. Mohammed, M. Abdulwahab, and E. T. Dauda, “Properties evaluation of shielded metal arc welded medium carbon steel material.,” Int J Innov Res Sci Eng Technol, vol. 2, no. 8, pp. 3351–3357, 2013.

[20] B. Sharma and S. Goyal, “Parametric Optimization of Shielded Metal Arc Welding of Milsd Steel (MS) 2062 using Taguchi Method,” ADR Journals, vol. 3, no. 3. pp. 11–18, 2016.

[21] I. S. Asibeluo and E. Emifoniye, “Effect of Arc Welding Current on the Mechanical Properties of A36 Carbon Steel Weld Joints,” SSRG International Journal of Mechanical Engineering, vol. 2, no. 9, pp. 79–87, 2015.

[22] J. O. O. * et Al, “Correlation between Process Variables in Shielded Metal-Arc Welding (SMAW) Process and Post Weld Heat Treatment (PWHT) on Some Mechanical Properties of Low Carbon Steel Welds,” Journal of Minerals and Materials Characterization and Engineering, vol. 11, no. 09, pp. 896–903, 2012, doi: 10.4236/jmmce.2012.119085.

[23] M. E, J. Nehru, E. College, A. Shukla, and V. S. Joshi, “Experimental Study of Shielded metal Arc Welding Parameter on Weld Strength for AISI 1020 Using Response Surface Methodology,” no. 9, pp. 1123–1126, 2017.

[24] R. Chiong, N. Khandoker, S. Islam, and E. Tchan, “Effect of SMAW parameters on microstructure and mechanical properties of AISI 1018 low carbon steel joints: An experimental approach,” IOP Conf Ser Mater Sci Eng, vol. 495, no. 1, 2019, doi: 10.1088/1757-899X/495/1/012093.

[25] D. Pathak, R. P. Singh, S. Gaur, and V. Balu, “Experimental investigation of effects of welding current and electrode angle on tensile strength of shielded metal arc welded low carbon steel plates,” Mater Today Proc, no. xxxx, pp. 1–3, 2020, doi: 10.1016/j.matpr.2020.01.146.

[26] S. H. Zoalfakar and A. A. Hassan, “Analysis and Optimization of Shielded Metal Arc Welding Parameters on Mechanical Properties of Carbon Steel Joints by Taguchi Method,” no. 01, pp. 1431–1444, 2017.

[27] E. Widodo, I. Iswanto, M. A. Nugraha, and K. Karyanik, “Electric current effect on mechanical properties of SMAW-3G on the stainless steel AISI 304,” MATEC Web of Conferences, vol. 197, pp. 1–4, 2018, doi: 10.1051/matecconf/201819712003.

[28] D. Kumar, M. Dharamvir, and *, “Study and Analysis of the Effect of Welding Process on Distortion With 304L Stainless Steel Weld Joints,” vol. 6, no. 2, pp. 212–216, 2017.

[29] A.K.Rude and Pimpalgaonkar, “Optimization Of Process Parameter In Hardfacing By Shield Metal Arc Welding (SMAW),” International Research Journal of Engineering and Technology (IRJET), vol. 05, no. 01, pp. 232–236, 2018.

[30] R. Selvam and S. Jacob, “Experimental investigation and analysis of SMAW processed carbon steel pipes,” International Journal of Mechanical and Production Engineering Research and Development, vol. 8, no. 5, pp. 29–40, 2018, doi: 10.24247/ijmperdoct20185.

[31] L. S. Sisira and K. Weeraskaralage, “Optimization of Shielded Metal Arc Welding (SMAW) process for mild steel Optimization of Shielded Metal Arc Welding (SMAW) process for mild steel,” Journal ENGINEER, no. August, 2019, doi: 10.13140/RG.2.2.23458.58560.

[32] D. Benne and D. Choudhary, “Experimentation and Analysis of Strength and Microstructural Parameters of Mild Steel Specimen Hardfaced by Chromium Zedalloy-350 Using Shielded Metal Arc Welding (SMAW) Process .,” vol. 2, no. 1, pp. 1–5, 2018.

[33] S. I. Talabi, O. B. Owolabi, J. A. Adebisi, and T. Yahaya, “Effect of welding variables on mechanical properties of low carbon steel welded joint,” Advances in Production Engineering And Management, vol. 9, no. 4, pp. 181–186, 2014, doi: 10.14743/apem2014.4.186.

[34] U. S. Patil and M. S. Kadam, “Microstructural analysis of SMAW process for joining stainless steel 304 with mild steel 1018 and parametric optimization by using response surface methodology,” Mater Today Proc, vol. 44, pp. 1811–1815, 2021, doi: 10.1016/j.matpr.2020.12.008.

[35] M. Khan, M. W. Dewan, and M. Z. Sarkar, “Effects of welding technique, filler metal and post-weld heat treatment on stainless steel and mild steel dissimilar welding joint,” J Manuf Process, vol. 64, no. December 2020, pp. 1307–1321, 2021, doi: 10.1016/j.jmapro.2021.02.058.

[36] M. A. Rojas Nova, L. M. Calderon Vergel, A. D. Pertuz Comas, and O. Bohorquez Becerra, “Efecto de la velocidad de avance en procesos de soldadura por arco eléctrico usando el método de elementos finitos,” Ciencia en Desarrollo, vol. 12, no. 2, pp. 67–72, 2021, doi: 10.19053/01217488.v12.n2.2021.13419.

[37] M. Matuszewski, “Modeling of 3D temperature field in butt welded joint of 6060 alloy sheets using the ANSYS program,” IOP Conf Ser Mater Sci Eng, vol. 659, no. 1, 2019, doi: 10.1088/1757-899X/659/1/012034.

[38] A. M. Sajeeb, “Parametric studies on weld penetration on plate of aluminium alloy 6061-T6 using FEM simulation,” Applied Mechanics and Materials, vol. 367, pp. 90–95, 2013, doi: 10.4028/www.scientific.net/AMM.367.90.

[39] A. Boudiaf and M. E. A. Djeghlal, “Modeling and Numerical Simulation of Thermal Cycles During GTAW Welding,” SSRN Electronic Journal, no. November, pp. 4–10, 2019, doi: 10.2139/ssrn.3389786.

[40] M. Cronje, “Finite Element Modelling of Shielded Metal Arc Welding,” no. December, pp. 1–110, 2005.

[41] “S355J2(+N) / 1.0570(dubl) - SteelNumber - Chemical composition, equivalent, properties.” Accessed: Jan. 29, 2023. [Online]. Available: http://www.steelnumber.com/en/steel_composition_eu.php?name_id=850

[42] “Ovako S355J2 S355J2(M) Steel, +AR.” Accessed: Jan. 29, 2023. [Online]. Available: https://www.matweb.com/search/datasheet.aspx?matguid=3c36b268408a4cc1ae7f789bd605d6c6&ckck=1

[43] “ISO - ISO 9692-1:2013 - Welding and allied processes — Types of joint preparation — Part 1: Manual metal arc welding, gas-shielded metal arc welding, gas welding, TIG welding and beam welding of steels.” Accessed: Feb. 26, 2023. [Online]. Available: https://www.iso.org/standard/62520.html

[44] K. Sripriyan, M. Ramu, P. R. Thyla, and K. Anantharuban, “Weld bead characterization of flat wire electrode in gmaw process part II: a numerical study,” Journal of Mechanical Science and Technology, vol. 35, no. 6, pp. 2615–2622, 2021, doi: 10.1007/s12206-021-0532-1.

[45] N. U. Dar, E. M. Qureshi, and M. M. I. Hammouda, “Analysis of weld-induced residual stresses and distortions in thin-walled cylinders,” Journal of Mechanical Science and Technology, vol. 23, no. 4, pp. 1118–1131, 2009, doi: 10.1007/s12206-008-1012-6.

[46] G. Fu, J. Gu, M. I. Lourenco, M. Duan, and S. F. Estefen, “Parameter determination of double-ellipsoidal heat source model and its application in the multi-pass welding process,” Ships and Offshore Structures, vol. 10, no. 2, pp. 204–217, 2015, doi: 10.1080/17445302.2014.937059.

[47] A. Kiran, Y. Li, J. Hodek, M. Brázda, M. Urbánek, and J. Džugan, “Heat Source Modeling and Residual Stress Analysis for Metal Directed Energy Deposition Additive Manufacturing,” Materials, vol. 15, no. 7, 2022, doi: 10.3390/ma15072545.

[48] J. Zhou and H. L. Tsai, Welding heat transfer. Woodhead Publishing Limited, 2005. doi: 10.1533/9781845690939.1.32.

[49] T. F. Flint, J. a Francis, and J. R. Yates, “Analytical solutions of the transient thermal field induced in finite bodies with insulating and convective boundary conditions subjected to a welding heat source,” 2013.

[50] J. Goldak, A. Chakravarti, and M. Bibby, “A new finite element model for welding heat sources,” Metallurgical Transactions B, vol. 15, no. 2, pp. 299–305, 1984, doi: 10.1007/BF02667333.

[51] Material Welding, “What is efficiency in welding & welding efficiency for SMAW, GMAW,TIG, FCAW and SAW?,” 2022, [Online]. Available: https://www.materialwelding.com/what-is-efficiency-in-welding-welding-efficiency-for-smaw-gmawtig-fcaw-and-saw/

[52] P. Vigneshwaran and M. P. Prabakaran, “Weld Strength Optimization by using Box-Behnken Design,” no. April 2014, 2019, [Online]. Available: www.ijert.org

[53] M. Alhajabdalla, H. Mahmoud, M. S. Nasser, I. A. Hussein, R. Ahmed, and H. Karami, “Application of response surface methodology and box-behnken design for the optimization of the stability of fibrous dispersion used in drilling and completion operations,” ACS Omega, 2021, doi: 10.1021/acsomega.0c04272.

[54] N. Ferreira et al., “Application of response surface methodology and box–behnken design for the optimization of mercury removal by Ulva sp.,” J Hazard Mater, vol. 445, no. November 2022, 2023, doi: 10.1016/j.jhazmat.2022.130405.

[55] S. L. C. Ferreira et al., “Box-Behnken design: An alternative for the optimization of analytical methods,” Anal Chim Acta, vol. 597, no. 2, pp. 179–186, 2007, doi: 10.1016/j.aca.2007.07.011.

[56] P. Sathiya, P. M. Ajith, and R. Soundararajan, “Genetic algorithm based optimization of the process parameters for gas metal arc welding of AISI 904 L stainless steel,” Journal of Mechanical Science and Technology, vol. 27, no. 8, pp. 2457–2465, 2013, doi: 10.1007/s12206-013-0631-8.

[57] H. Cui et al., “Numerical Simulation of the Interaction Between Arc Plasma and Molten Slag in Electric Arc Furnace for High-Titania Slag Smelting,” Metallurgical and Materials Transactions B: Process Metallurgy and Materials Processing Science, vol. 54, no. 4, pp. 1687–1704, Aug. 2023, doi: 10.1007/S11663-023-02775-8/METRICS.

[58] S. H. Zargar, M. Farahani, and M. K. B. Givi, “Numerical and experimental investigation on the effects of submerged arc welding sequence on the residual distortion of the fillet welded plates,” Proc Inst Mech Eng B J Eng Manuf, vol. 230, no. 4, pp. 654–661, 2016, doi: 10.1177/0954405414560038.

[59] “S355J2 steel plate,S355J2 sheet,S355J2 coil - Carbon steel”, [Online]. Available: https://www.steelss.com/Carbon-steel/s355j2.html

[60] M. M. Ali, F. Dave, R. Sherlock, A. Mcilhagger, and D. Tormey, “Simulated Effect of Carbon Black on High Speed Laser Transmission Welding of Polypropylene With Low Line Energy,” Front Mater, vol. 8, no. September, pp. 1–14, 2021, doi: 10.3389/fmats.2021.737689.

[61] S. Kannan, S. S. Kumaran, and L. A. Kumaraswamidhas, “Optimization of friction welding by taguchi and ANOVA method on commercial aluminium tube to Al 2025 tube plate with backing block using an external tool,” Journal of Mechanical Science and Technology, vol. 30, no. 5, pp. 2225–2235, 2016, doi: 10.1007/s12206-016-0432-y.

[62] F. Reyes-Calderón, R. Vences-Hernández, J. A. Salazar-Torres, H. J. Vergara-Hernández, I. Aguilera-Navarrete, and V. Pérez-González, “Parameter optimization: Force (F), time (T) and current intensity (I), in the RSW welding process of DP-290 steel plates using the taguchi method,” Soldagem e Inspecao, vol. 23, no. 2, pp. 157–167, 2018, doi: 10.1590/0104-9224/SI2302.04.

[63] S. C. Bodkhe and D. R. Dolas, “Optimization of Activated Tungsten Inert Gas Welding of 304L Austenitic Stainless Steel,” Procedia Manuf, vol. 20, pp. 277–282, 2018, doi: 10.1016/j.promfg.2018.02.041.

[64] B. Trembach, A. Grin, M. Turchanin, N. Makarenko, O. Markov, and I. Trembach, “Application of Taguchi method and ANOVA analysis for optimization of process parameters and exothermic addition (CuO-Al) introduction in the core filler during self-shielded flux-cored arc welding,” International Journal of Advanced Manufacturing Technology, vol. 114, no. 3–4, pp. 1099–1118, 2021, doi: 10.1007/s00170-021-06869-y.

[65] S. Karaoğlu and A. Seçgin, “Sensitivity analysis of submerged arc welding process parameters,” J Mater Process Technol, vol. 202, no. 1–3, pp. 500–507, Jun. 2008, doi: 10.1016/J.JMATPROTEC.2007.10.035.

[66] Z. Chen, C. Li, X. Han, X. Gao, and H. Gao, “Sensitivity analysis of the MIG welding process parameters based on response surface method,” J Adhes Sci Technol, vol. 35, no. 6, pp. 590–609, 2021, doi: 10.1080/01694243.2020.1816778.

[67] J. Luukkonen, A. Pohjonen, S. Louhenkilpi, J. Miettinen, M. J. Sillanpää, and E. Laitinen, “Gradient Boosted Regression Trees for Modelling Onset of Austenite Decomposition During Cooling of Steels,” Metallurgical and Materials Transactions B: Process Metallurgy and Materials Processing Science, vol. 54, no. 4, pp. 1705–1724, 2023, doi: 10.1007/s11663-023-02782-9.

[68] P. Merico, M. Faccoli, and G. Cornacchia, “Analysis of Ancient Slag Inclusion-Metal Systems as a Method to Disclose Processing Thermo-chemical Parameters: The Case Study of a Medieval Lombard Steel Bar from Northern Italy,” Metallurgical and Materials Transactions B: Process Metallurgy and Materials Processing Science, vol. 54, no. 3, pp. 1408–1421, 2023, doi: 10.1007/s11663-023-02769-6.

[69] Y. Zhang, H. Liu, T. Coetsee, Z. Wang, and C. Wang, “Identifying Oxygen Transfer Pathways During High Heat Input Submerged Arc Welding: A Case Study into CaF2-SiO2-CaO-TiO2 Fluxes,” Metallurgical and Materials Transactions B: Process Metallurgy and Materials Processing Science, vol. 54, no. 6, pp. 2875–2880, Dec. 2023, doi: 10.1007/S11663-023-02922-1/METRICS.

[70] B. Kiran, K. Mishra, Y. R. Singh, and D. Nagaraju, “Structural and thermal analysis of butt joint GTAW of similar and dissimilar materials with distinct groove angles through simulation and mathematical modelling,” FME Transactions, vol. 48, no. 3, pp. 667–680, 2020, doi: 10.5937/FME2003667B.

[71] J. Wang, H. Yuan, N. Ma, and H. Murakawa, “Recent research on welding distortion prediction in thin plate fabrication by means of elastic FE computation,” Marine Structures, vol. 47, pp. 42–59, 2016, doi: 10.1016/j.marstruc.2016.02.004.

Author contribution:

1. Conception and design of the study
2. Data acquisition
3. Data analysis
4. Discussion of the results
5. Writing of the manuscript
6. Approval of the last version of the manuscript

SFH has contributed to: 1, 2, 3, 4, 5 and 6.

SAK has contributed to: 1, 2, 3, 4, 5 and 6.

AS has contributed to: 1, 2, 3, 4, 5 and 6.

MNB has contributed to: 1, 2, 3, 4, 5 and 6.

AM has contributed to: 1, 2, 3, 4, 5 and 6.

AN has contributed to: 1, 2, 3, 4, 5 and 6.

MMA has contributed to: 1, 2, 3, 4, 5 and 6.

SN has contributed to: 1, 2, 3, 4, 5 and 6.

Acceptance Note: This article was approved by the journal editors Dr. Rafael Sotelo and Mag. Ing. Fernando A. Hernández Gobertti.